Nanoscale

PAPER

View Article Online
View Journal | View Issue

Cite this: *Nanoscale*, 2017, **9**, 9386

Resistive switching mechanism of GeTe–Sb_2Te_3 interfacial phase change memory and topological properties of embedded two-dimensional states†

Hisao Nakamura, *[a] Ivan Rungger,[b] Stefano Sanvito,[c] Nobuki Inoue,[a] Junji Tominaga[d] and Yoshihiro Asai[a]

A theoretical study of an interfacial phase change memory made of a GeTe–Sb_2Te_3 superlattice with W electrodes is presented to identify the high and low resistance states and the switching mechanism. The ferro structure of the GeTe layer block in the Te–Ge–Te–Ge sequence can be in the low resistance state only if the SET/RESET mode consists of a two step dynamical process, corresponding to a vertical flip of the Ge layer with respect to the Te layer, followed by lateral motion driven by thermal relaxation. The importance of spin–orbit coupling at the GeTe/Sb_2Te_3 interface to the "bias polarity-dependent" SET/RESET operation is shown, and an analysis of the two-dimensional states confined at the GeTe/Sb_2Te_3 interface inside the resistive switching layer is presented. Our results allow us to propose a phase diagram for the transition from a topologically nontrivial to a trivial gap state of these two-dimensional compounds.

Received 16th May 2017,
Accepted 20th June 2017

DOI: 10.1039/c7nr03495d

rsc.li/nanoscale

Introduction

Nonvolatile memories have become one of the major research targets in functional electronic device research because of the society's needs for battery-less information storage and for more efficient CPUs based on memristic or neuronic computations.[1] The Phase Change Memory (PCM) is one of the candidates for next-generation nonvolatile memory technologies due to its good retention and less variation in resistance values over many read/write cycles.[2,3] Chalcogenide crystals have been widely used as phase-change materials, which switch between crystalline and amorphous phases. Some of them have already been in the market as memory materials for optical memories, such as with the Digital Versatile Disc Random Access Memory (DVD-RAM).[4,5] In applications as electric nonvolatile memory, alloys of Ge, Sb and Te (GST) are a promising material for the resistive switching layer (RSL) of the PCM device, where the resistance switches by Joule heating driven by the current flow. However, this heating-based switching mechanism relies on a high entropy loss, and it is inherently not suitable for ultra-low power operation and fast-switching, which limits the future applicability of this standard PCM technology.

Recently, a new phase transition mechanism was proposed for the superlattice structure of GST, which consists of an alternate staking of hexagonal Sb_2Te_3 quintuple layers (QL) and GeTe layers.[6,7] The unit is represented by $(Sb_2Te_3)_m(GeTe)_n$, where the indices characterize the numbers of QL blocks and GeTe layers, (m,n), is tunable with advanced fabrication techniques.[8] From now on, we denote the QL block $(Sb_2Te_3)_m$ as $(QL)_m$ for simplicity. In the GST superlattice (GST-SL) the phase transition occurs between two different crystalline phases, as shown in ref. 8 and 9. According to a recent study, the loss of entropy of GST-SL is reduced by 95% compared to that of the related alloy, so that a lower power SET/RESET operation is feasible.[7]

There have been several experimental indications of resistive switching in the devices including GST-SL films as RSL. In order to emphasize the difference in the "phase transition" mechanism of superlattices compared to that of standard PCMs, the former is often called interfacial PCM (iPCM). Clearly, iPCM has the great potential advantage of being power-saving and high speed in the SET/RESET process when compared to standard PCMs, and possibly it is also amenable to high-integration. However, the atomistic structures of the high and low resistance states (HRS and LRS, respectively) are not fully understood. Furthermore, the dynamics of the structural change is still under debate. For an instance, it is

[a]*CD-FMat, National Institute of Advanced Industrial Science and Technology (AIST), 1-1-1 Umezono, Tsukuba Central 2, Tsukuba, Ibaraki 305-8568, Japan. E-mail: hs-nakamura@aist.go.jp*
[b]*National Physical Laboratory, Teddington, TW11 0LW, UK*
[c]*School of Physics, AMBER and CRANN Institute, Trinity College, Dublin 2, Ireland*
[d]*NeRI, National Institute of Advanced Industrial Science and Technology (AIST), 1-1-1 Higashi, Tsukuba Central 5, Tsukuba, Ibaraki 305-8565, Japan*
†Electronic supplementary information (ESI) available. See DOI: 10.1039/c7nr03495d

not clear whether the trigger for the SET and RESET operations is determined by electric field-driven effects in the bipolar voltage sweep or whether it is current-driven. If a field-driven switching realizes sufficiently low resistance, power consumption may be drastically suppressed because of the reduced electric current applied for the switching.[10] Hence further power-saving may become possible.

Presently, the inverted Petrov phase, whose GeTe layer block takes a Te–Ge–Ge–Te sequence and (referred to as IP structure), is suggested as HRS by first-principles band structure calculations, as well as by high-angle annular dark field transmission electron microscopy (HAADF-TEM) images of the iPCM device.[8] To the best of our knowledge, only the scenario where the crystal structure of the GeTe layers changes without strong layer mixing with the QL explains the observed cyclic and the enthalpy-loss resistive switching of iPCM.[7,8,11] Here we note that fabrication of GST-SL, the Ge (and/or Te) vacancy layer is introduced into GeTe(111) of disordered rock-salt structure in order to stack GeTe block.[12]

In the present study, we consider only small values of (m,n) (typically, $m = 2$, $n = 2$). Very recently, strong interlayer mixing of QL blocks and GeTe layers in GST-SL, which partially breaks the perfect reciprocal stacking, has been reported by a few research groups.[13,14] However, the stability of the ordered structure depends on the value of (m,n) and on the fabrication process.[15] As long as the values of m and n are sufficiently small, the reciprocal $(QL)_m(GeTe)_n$ stacking is possible.[16] As stated above, the structure of GeTe layers in GST-SL is GeTe (111) rock salt including vacancy layers. The vacancy layer makes the van der Waals (vW) gap and it provides the space for coherent dynamics of Ge and Te atoms, which is necessary for the phase transition without melt or interlayer mixing. In the standard PCM of GST bulk, vacancies play an important role to pin the Fermi level then they change resistance.[17] Hence the role of vacancies between the iPCM and standard PCMs are different. Further introduce of vacancies into GST-SL will trigger corruption of the reciprocal GST-SL and make strong interlayer mixing. Then the resistive switching mechanism changes to that of standard PCMs. Thus it is reasonable to expect that the HRS and LRS of the iPCM device are characterized by the structural phase change in GeTe layers of the GST-SL. We set our theoretical models of the iPCM without including further vacancies or interlayer mixing structures.[18]

One of the main questions we address in this work regarding the emerging iPCM devices concerns the unknown detailed atomistic structures of the GeTe layers of the LRS, and the related switching mechanism, which can be either bias polarity-dependent (field-driven) or independent (current-driven) SET/RESET operation as described above.[10] Though previous theoretical analyses are based only on the bulk band structures of the GST-SL,[19–21] they are not necessarily related to the transport properties of the iPCM device. The effects of the contacts between the RSL and the electrodes, difference of the Fermi levels, bias voltage *etc.* often dominate the electric transport mechanisms, in particular, nano-scale devices.[22,23] In the present study, we carry out high-quality quantum transport calculations to obtain the current–voltage (I–V) characteristics of the iPCM device. Then we show a detailed analysis to resolve the nature of the LRS. Tungsten is frequently used as the electrode in experiments due to the formation of good contacts with the RSL,[19] and therefore we use it in our calculations as well. By analyzing the LRS we then determine whether a field-driven operation is possible in the device structure.

There are two candidates for the GeTe crystalline phases of the LRS. These are called the Petrov phase[19] and the Ferro-GeTe phase.[24,25] The former presents the Ge–Te–Te–Ge sequence, while the latter has Te–Ge–Te–Ge order (or equivalently, Ge–Te–Ge–Te). In previous studies, the SET (RESET) process has been assumed to correspond to a one-step vertical flip motion of a Ge layer from (to) the inverted Petrov to (from) the Petrov or Ferro-GeTe phase. Very recently, Yu and Robertson suggested a two-step mechanism, where the phase transitions consist of a vertical flip of Ge, followed by lateral motion.[26] Thus, the Petrov (Ferro-GeTe) phase is further classified by the nature of the vertical flip of the Ge layer in the IP structure, which is termed as P(v) [FGT(v)] for the vertical flip only, while that followed by lateral motion is denoted as P(vl) [FGT(vl)]. Here we identify the dominant LRS from these possible structures by using first-principles transport calculations.

The second question addressed in this study concerns how the nature of the two-dimensional (2D) states at the QL/GeTe interfaces in the device and how this affects the conductance. Several research groups have recently argued that a phase transition between topologically trivial and non-trivial states occurs by varying the number of QL blocks and GeTe layers.[27] First principles band structure calculations for bulk GST-SL showed that the inverted Petrov phase can be a strong three-dimensional (3D) topological insulator (TI), depending on the numbers (m,n) in $(QL)_m(GeTe)_n$.[21,28,29] However, the surface state of bulk GST-SL is difficult to utilize for device applications. In iPCM devices the outermost surfaces of the GST-SL RSL are connected to the electrodes, and hence the surface states are usually strongly coupled to them. This changes significantly the nature of the GST-SL surface states. On the contrary, the QL/GeTe interface states separate the TI $(QL)_m$ blocks from the usually normal insulator (NI) $(GeTe)_n$ blocks, which in the superlattice act as bridges between the TI blocks. These are robust, since they are the edge states "built-in" inside the device, which makes them very attractive for device applications. According to the argument of the previous studies[21,30,31] for bulk systems, a topological transition in the multilayers of TIs and NIs takes place by closing the energy gap at the Dirac point. In this study, we show that a similar topological transition takes place also inside the iPCM device, including the metal electrodes, by evaluating the quasi-particle band dispersion of this interface state. This allows us to evaluate the phase diagram by introducing an effective Hamiltonian model with which we discuss the topological phase change of the iPCM device. Finally, we clarify the relation between the interface band structure and transport property of the iPCM device by presenting the k-point dispersion of the transmission coefficient.

Structure of GST-SL and model of iPCM device

We use the notation $[(m,n)]$ to represent the unit cell of the reciprocally stacked $(QL)_m(GeTe)_n$ GST-SL. When a number, l, of such units are stacked, we refer to the resulting film as $[(m,n)]_l$. In this notation the GST-SL bulk form of the $[(m,n)]$ unit block is $[(m,n)]_\infty$. Following the discussion of ref. 26, we investigate the IP structure for the HRS and examine the four possible LRS structures: P(v), P(vl), FGT(v), and FGT(vl). The structures of the $[(2,2)]$ unit cell for all of the above crystal phases are shown in Fig. 1, where we have also labeled the individual atoms. The parameters of these bulk GST-SL $[(2,2)]$ crystalline structures obtained by density functional theory (DFT) are summarized in the ESI, Table SI.1.† The relative differences between the total energies per the unit cell are lower than 0.5 eV for the IP, P(v), P(vl), FGT(v) and FGT(vl) structures. Thus, all structures listed here can be considered as possible candidates for the LRS. The difference of a- (and b-axis) length between these unit cells, whose directions are parallel to the interface, is negligible (~1.4%) for the considered phases, so that we can take the same a and b-axis lattice constants to construct all the device models of HRS and LRS.

When setting up the iPCM device structures, we have to include the GST-SL film as RSL and the electrode materials on the left and right side explicitly. The RSL is made of $[(2,2)]_l(QL)_2$, where the last $(QL)_2$ block is introduced to obtain symmetric junction. We then take bcc W(111) as the electrodes: thus the device structure is expressed as $W/[(2,2)]_l(QL)_2/W$.

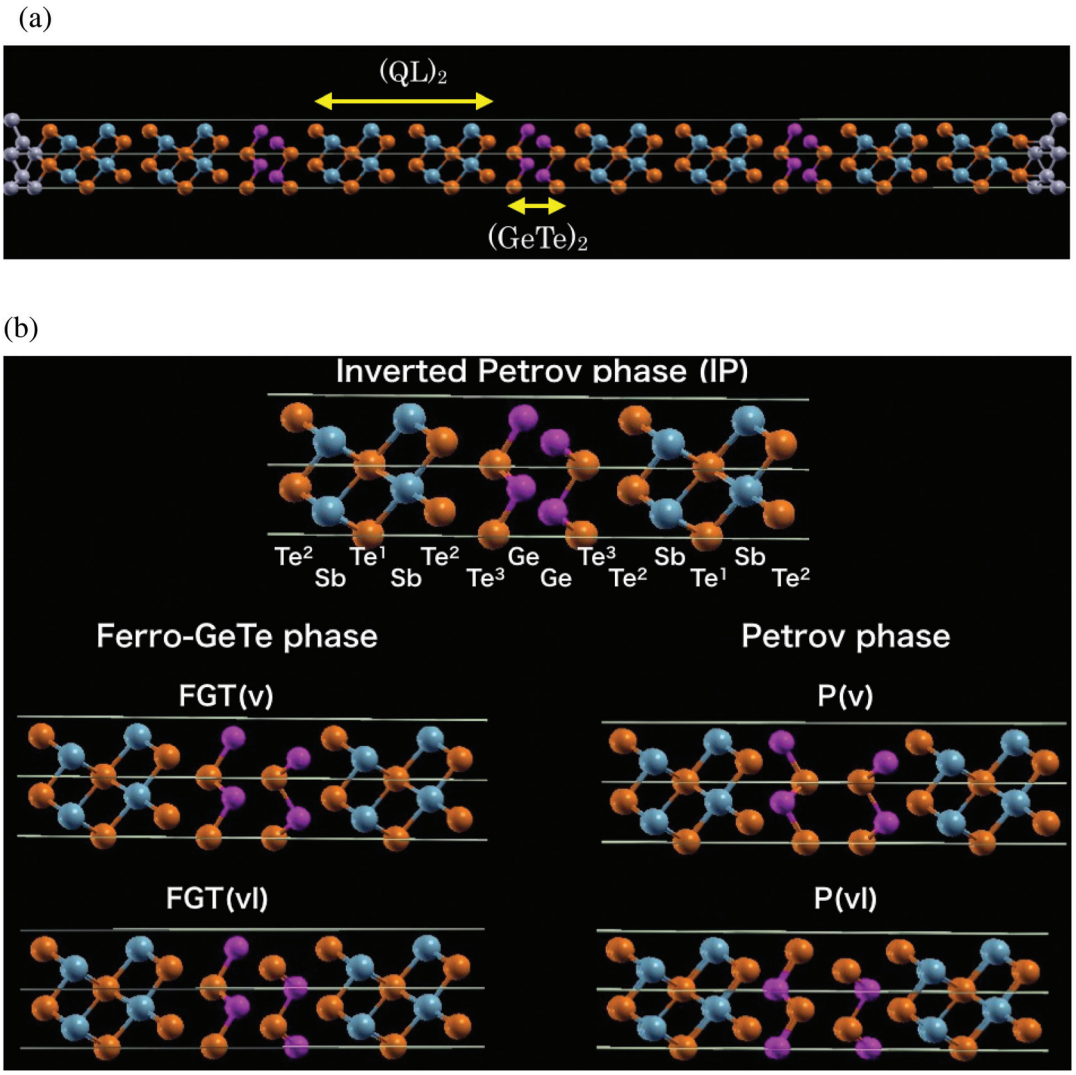

Fig. 1 Model structures of iPCM device. (a) The structure of the device model $W/[(QL)_2(GeTe)_2]_3(QL)_2/W$ of the inverted-Petrov phase, where only a few top layers are shown as the electrodes. (b) The detail structures of [(2,2)] GST-SL unit. The top panel is inverted Petrov (IP). The number index is labeled to each atom for a reference. The lower left panel consists of Ferro-GeTe phase of vertical flip structure (FGT(v)) and vertical flip followed by lateral motion (FGT(vl)). The lower right panel represents Petrov phase of vertical flip structure (P(v)) and that followed by lateral motion (P(vl)). The purple, brown, and thin blue balls represents Ge, Te, and Sb atoms, respectively. The grey balls are W atoms.

Fourteen atomic layers of W are included in our simulation cell at both the left-hand and right side. In order to perform the calculation of the *I–V* characteristics, we introduce the minimum device model by setting $l = 3$, so that the setup corresponds to W/$[(2,2)]_3(QL)_2$/W, as shown in Fig. 1. Next, we determine the atomic positions of the W/$[(2,2)]_3(QL)_2$/W structure, where each GeTe layer is set to the IP structure, and the lattice constant of the *a* and *b* axes is fixed at 4.19 Å. We relax all atoms of the RSL and of the two innermost W atomic layers. We also change the electrode-gap distance, which is defined as the distance between the third W layer of left and right electrodes. We find that the total energy of the entire W/$[(2,2)]_3(QL)_2$/W system of the IP structure is lower when the electrode-gap distance is 110.5 Å. However, the change of the total energy varies only by 0.2 eV when extending the electrode-gap distance up to 112.9 Å. This result is consistent with the previous experimental and theoretical predictions that neighboring QLs inside the $(QL)_m$ block, and/or of GeTe and neighboring QLs, are bound by weak interactions. Since the optimized values of the *c* axis length differ in each other structures, we fix the electrode-gap distance to 112.9 A. This approximately corresponds to taking the average *c*-axis length for the IP and P(v) structures. The resulting bond lengths of the atoms in the [(2,2)] unit of W/$[(2,2)]_3(QL)_2$/W are listed in the ESI (Table SI.2†). We also determine the relaxed atomic positions in the RSL for P(v), P(vl), FGT(v), and FGT(vl), at the electrode-gap distance of 112.9 A. Here we note that the structure of each QL, and the distance of the neighboring QLs in the $(QL)_2$ block are almost unchanged for all the present phases. To distinguish the structures of the [(2,2)] unit obtained by the geometry optimization procedure for bulk GST-SL from those used for the minimum device model, we represent the latter as $[(2,2)_{ref}]$. Hence, our minimum device model is rewritten as W/$[(2,2)_{ref}]_3(QL)_2$/W, and that identifies the atomic positions and the distances of the neighboring QLs and QL/GeTe. In the next section, we apply electric transport calculations to the above minimum device models by using the nonequilibrium Green's function method combined with DFT (NEGF-DFT).[32–34]

Electric transport properties and identification of the low resistance state

For a practical low-power nonvolatile memory, a sufficiently large ratio between ON (in the LRS) and OFF current (in the HRS) is required. Hence, we focus on the *I–V* curves in the low voltage regime, typically [−0.5, 0.5] volt. It is well known that the $(QL)_m$ films are TIs, and that this effect is caused by the large spin–orbit (SO) interactions of the Ge and Te atoms. We therefore perform the NEGF-DFT calculations including SO coupling.

In Fig. 2(a), the calculated *I–V* curves of our minimum device models for all the considered structures are shown within the zero-bias limit approximation. Here the 0-bias transmission coefficient is integrated over the bias window to obtain the current and the effect of the voltage drop between the electrodes is neglected. The lowest calculated current is given by the IP structure. Calculations of the electronic band structures of bulk GST-SL were examined and the IP structure was assigned as HRS in previous studies. However, the electronic structure of only the RSL does not necessarily correlate with the transport property of the device. Our *I–V* calculation agrees with the above conclusion and gives us direct evidence that the IP structure is HRS. We find that the transition from IP to P(v) gives the highest ON/OFF current ratio, so that the optimal LRS is P(v), when we focus on reading/writing information without errors by low electric current. Since the structural transition from IP to P(v) requires a symmetric vertical flip of two Ge layers, as shown in Fig. 1, resistive switching *via* the transition to P(v) operates in a nonpolar mode, and consequently is expected to be driven by the current Joule heating effect. Importantly, the electric current of the FGT(v) structure is as low as that of the IP, which means that FGT(v) cannot be the LRS in the low bias regime. These *I–V* characteristics obtained by the vertical flip motion of the IP imply that the SET/RESET operation is due to a one-step dynamics if the SET/RESET is nonpolar.

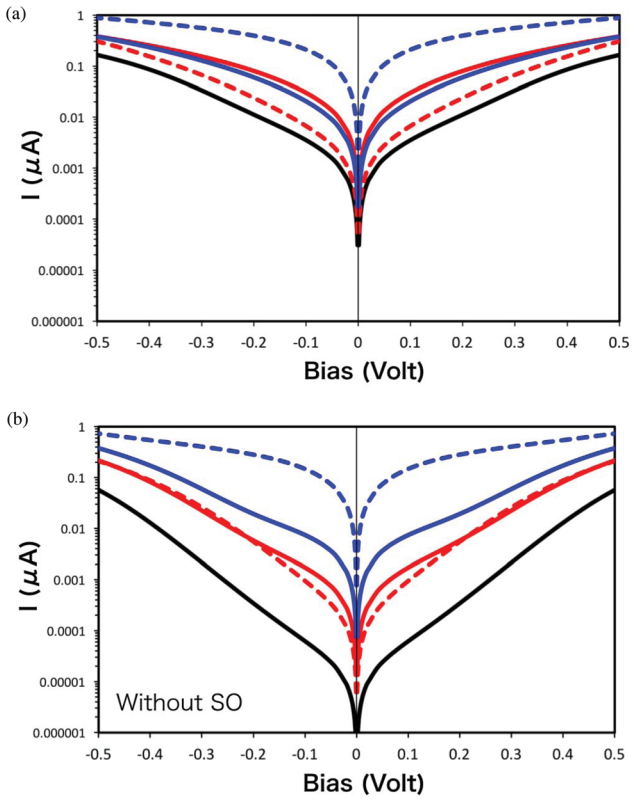

Fig. 2 Semi-log plot of *I–V* characteristics of (a) with SOC (b) without SOC, where voltage drop effects are omitted (*i.e.*, zero-bias approximation). The black solid, red dot, blue dot, red solid, and blue solid lines are IP, FGT(v), P(v), FGT(vl), P(vl) structures, respectively.

In contrast, the lateral diffusion of the Ge layer after the vertical flip motion suppresses the electric current of the Petrov phase, which we denote as P(vl) structure, while it increases the current of the Ferro-GeTe phase, which we denote as the FGT(vl) structure. We find that the difference in the *I*–*V* curves for P(vl) and FGT(vl) becomes much smaller than that between P(v) and FGT(v). The advantage of the Petrov phase as LRS is almost lost by the following lateral motion. Furthermore, the electric current of FGT(vl) is about 10 times larger than that of IP at $V = 0.2$ volt. These results therefore show that FGT(vl) can be the LRS. Recalling that the Ferro-GeTe phase is an anti-symmetric configuration, we expect the transition from IP to FGT(vl) to be bias polarity-dependent *i.e.*, field-driven, and we expect a two-step mechanism to be dominant for the SET/RESET process. Such a field-driven operation is possible when the device temperature is sufficiently high to trigger the thermal lateral relaxation.

In order to elucidate the effects of the SO coupling in the *I*–*V* characteristics we also carry out NEGF-DFT calculations without SO interaction, and the results are shown in Fig. 2(b). The general trends of the *I*–*V* characteristics of the inverted Petrov and Petrov phases are not sensitive to SO interaction, even though the SO coupling slightly enhances the magnitude of the total electric current. However, the SO significantly affects the Ferro-GeTe phase: by comparing the results with and without SO interaction we find that SO interaction provides distinct differences in the *I*–*V* profiles of the FGT(v) and FGT(vl) structures of the Ferro-GeTe phase. With the aim to identify the LRS, the above theoretical results show that the SO coupling plays an important role, where FGT(vl) is more conductive than FGT(v). Since only the Ferro-GeTe phase breaks the parity symmetry, a large Rashba effect is expected.[9,35] Thus we conclude that different *I*–*V* profiles of FGT(v) and FGT(vl) structures are caused by the different Rashba splitting in the iPCM device.

Next, we also verify the effect of including the voltage drop in the system by calculating fully self-consistent finite bias NEGF-DFT *I*–*V* curves. The resulting *I*–*V* characteristics are presented in Fig. 3. It can be seen by comparing to Fig. 2(a) that including the bias voltage has only minor effects on the transport properties. This implies that the Rashba effect induced by the bias polarity is weak in the present low-bias regime. Therefore, the proposed scenario that the bias polarity-independent (current-driven) operation is a one-step process, and the field-driven mode relates to a two-step dynamics is further confirmed by the robustness of the results also for self-consistent voltage calculations. The results of the finite biased *I*–*V* characteristics also show that robustness of our arguments to identify HRS and LRS. The NEGF-DFT calculation requires the charge neutrality condition only for the entire device. The local excess charge induced by voltage drop is included self-consistently. Very small difference of the results wit/without bias suggests that energy level shift by local excess charge is less important to determine HRS/LRS.

Here, we comment on the accuracy of the adopted first-principles method since the underestimation of band gap by

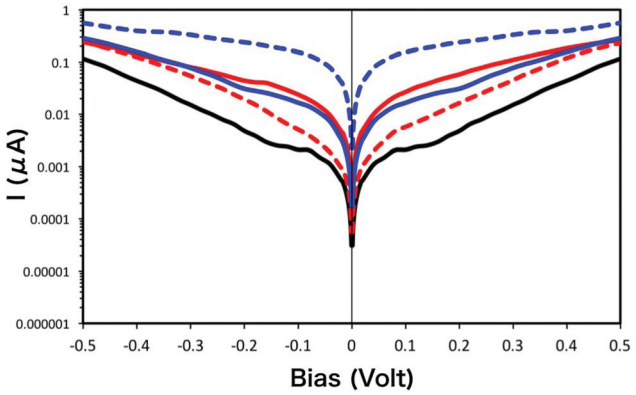

Fig. 3 Semi-log plot of *I*–*V* characteristics including SOC and voltage drop effects. The legend of the represented lines is same with that of Fig. 2.

DFT is often criticized (see Methods). To check the error of the adopted basis set and the exchange correlation functional, we calculate the band gap of Sb_2Te_3 rhombohedral and GeTe rock salt crystals. The results are 0.1 eV, and 0.45 eV, respectively while the experimental values are 0.2 eV, and 0.65 eV according to the literatures.[36,37] Accuracy is very reasonable for out purpose. Furthermore, as shown in Fig. 1, the structures of QL blocks of the IP, FGT(v), FGT(vl), P(v), and P(Vl) structures are quite similar, *i.e.*, the underestimation of band gap is less important that change of electronic states by structural change of GeTe layers. Thus the error of DFT does not give any change to our analysis to identify HRS and LRS.

Before closing this section we discuss the device scale dependence of the performance of resistive switching on the device scale by evaluating the results for different thicknesses of the RSL. In order to analyze the resistance ratio of the LRS (R_{LRS}) and HRS (R_{HRS}), we extend the structure by inserting six $[(2,2)_{ref}]$ units into our minimum device model $W/[(2,2)_{ref}]_3(QL)_2/W$. Hence, the resulting RSL is lengthened to $[(2,2)_{ref}]_{l\,=\,9}(QL)_2$. We only evaluate the results for the IP as HRS and, the P(v) and FGT(vl) structures as optimal LRS of the Petrov and Ferro-GeTe phases, respectively. The lengthened device structure is defined as $W/[(2,2)_{ref}]_9(QL)_2/W$. We can now take the differential resistance $(dI/dV)^{-1}$ at $V = 0.2$ volt as an indicative $R_{LRS(HRS)}$. When we assume that the LRS is P(v), then the resistive ratio, R_{LRS}/R_{HRS}, is 0.07 for $l = 3$, and 0.08 for $l = 9$, showing that the ratio is largely unchanged for different spacer lengths. The ratio is also independent to the number of l for FGT(vl), where the values are 0.24 for $l = 3$ and 0.23 for $l = 9$. The electric conductivity of nonmetallic films usually decreases exponentially as a function of the film thickness when the electric transport is tunneling and far from resonance.[38] If the coupling strength (transfer integral) between the neighboring QL and GeTe layers is strong, length dependence of R_{LRS} and R_{HRS} must be largely different and hence the ratio R_{LRS}/R_{HRS} must depend on l. Thus the found "device-scale independence" predicts that the GeTe layer perturbs the electronic couplings between the states of neighboring

QL blocks along the transport direction. Finally, we note that the calculated resistive ratio agrees well with experimental results, where the measured ratio is R_{LRS}/R_{HRS} is order of 0.1.[7,8]

Interfaces states and Dirac semi-metallic phase of iPCM devices

In this section, we analyze the topological properties and the interface states at the GeTe/QL interface of the RSL *inside* the device. It is known that the inverted Petrov phase of GST-SL can be a 3D strong TI when (m,n) is equal to (1,2) or (2,2).[21,28,29] The Z_2 topological invariant $\nu_0;(\nu_1,\nu_2,\nu_3)$ is 1;(100) for the former and 1;(001) for the latter.[28] Generally, the topologically non-trivial sates (Dirac cone band dispersion) are edge states, namely they are surface states facing vacuum. However, these surface states are not automatically preserved in the iPCM device cell, since the top/bottom RSL edge states are not exposed to vacuum, but are strongly mixed with the electronics structure of the metal electrodes. In contrast, the interface states inside iPCM, which are defined as the built-in 2D states of the QL and GeTe layers, are more interesting, since (1) the QL is a TI and its interaction with the GeTe layers is weak, and (2) the topological phase transition may provide an additional novel functionality to the device. In this section, we mainly focus on interface states of the inverted Petrov phase (IP structure), since only IP can be topologically insulating. In the following discussion we will explicitly mention if we refer to other structures.

First, we evaluate the 2D band dispersion of the surface states of bulk GST-SL, where the $[(2,2)_{ref}]$ unit cell structure is used to construct the RSL. We calculate rigorously the surface Green's function imposing a semi-infinite boundary condition by cleaving the layers of QL and GeTe (Surf-Te), and by cleaving the adjacent GeTe layers (Surf-Ge). Then we evaluate the projected density of states on the edge of the QL as a function of the energy, E, and $\vec{k}_{\parallel}$ point. The resulting contour plots shown in Fig. 4 correspond to the in-plane quasi-particle band structure of the interface states. In all cases, we found a linear band dispersion crossing the Γ point with the crossing point between 0.1 eV and 0.05 eV below the Fermi level, E_F, corresponding to the bulk GST-SL for Surf-Te and Surf-Ge. The linear surface band dispersion for both cleaving surfaces agrees with previous theoretical calculations of [(1,2)] bulk. However, there is an important qualitative difference in Dirac cone dispersions of Sur-Te for $[(2,2)_{ref}]$. The upper cone connected to the conduction band region and the lower one exist in the valence band region as in a standard TI for [(1,2)] as shown in ref. 28. On the contrary, the linear bands of Surf-Te of $[(2,2)_{ref}]$ do not connect to the upper quadratic band relating to the conduction band region. Note that the Kramers pair of Sur-Ge across the gap of valence and conduction band regions as a standard TI for both of [(1,2)] and $[(2,2,)_{ref}]$.

For comparison, we examine a strained GST-SL by elongating the c-axis lattice constant by 2.8% compared to that of

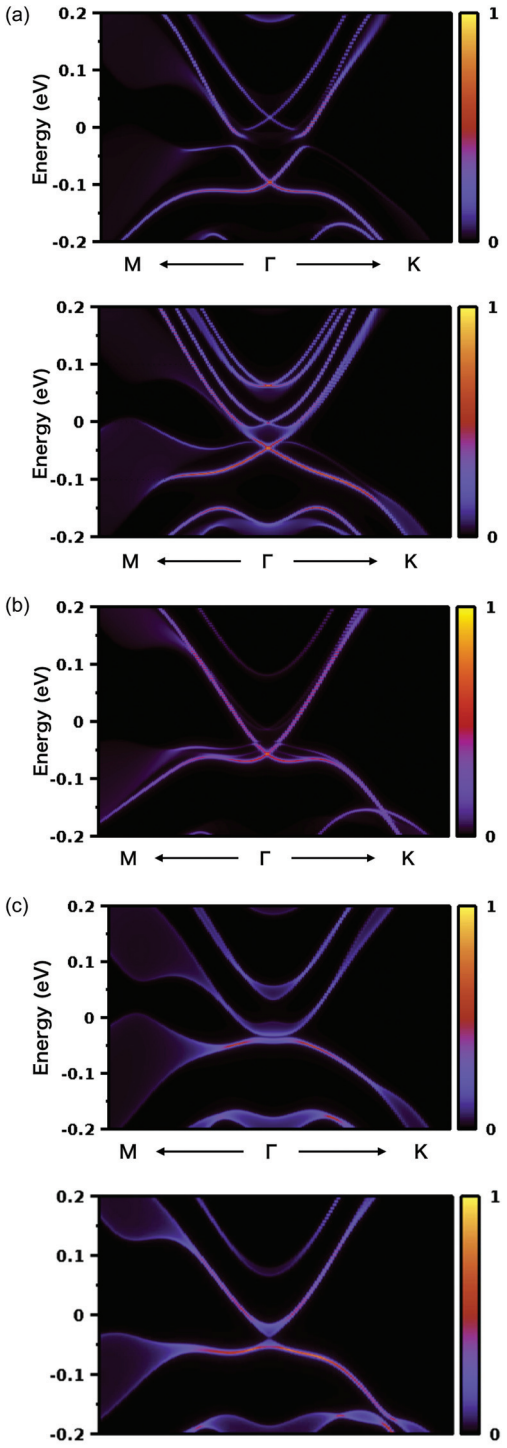

Fig. 4 The contour plots of the PDOS of the surface states and interface states for the inverted Petrov phase as a function of electron energy E and the wave vector $\vec{k}_{\parallel}$ (2D band dispersion). (a) Plot of the surface states of GST-SL bulk of $[(2,2)_{ref}]$ unit. The upper panel is the edge by cleaving QL and GeTe layers (Sur-Te) while the lower panel is the edge by cleaving the adjacent GeTe (Sur-Ge). (b) Plot of the surface states of GST-SL bulk of $[(2,2)_{elng}]$ unit by cleaving QL and GeTe layers (Sur-Te). (c) Plot of the interface states of the iPCM device. The upper panel is PDOS on the edge of the center QL in $W/[(2,2)_{ref}]_9(QL)_2/W$. The lower panel is that of $W/[(2,2)_{elng}]_9(QL)_2/W$. The zero of energy is set to E_F of GST-SL bulk for (a), (b) and that of electrode (W bulk) for (c). The unit of density of states is arbitrary.

$[(2,2)_{ref}]$. The changes in bond lengths due to the above strain are summarized in the ESI (Table SI.2†). We refer to this elongated GST-SL unit cell as $[(2,2)_{elng}]$. The surface states band dispersion of Surf-Te for $[(2,2)_{elng}]$ bulk are shown in Fig. 4(b). The states of Sur-Te of $[(2,2)_{elng}]$ show a clear Dirac cone located in the gap of the valence and conduction band regions, while that of $[(2,2)_{ref}]$ is in the gap of the valence band. The Dirac point is close to the Fermi energy, namely it is only 0.05 eV below E_F. These results lead to the prediction that the surface state is sensitive to strain along the *c*-axis when *m* and *n* are equal to 2. This is slightly different from the case of (m = 1, n = 2), because the surface state of [(1,2)] bulk is always topologically non-trivial up to 4% strain along *c*-axis, as shown in ref. 28. When the unit cell consists of two or more QL layers, the system contains two kinds of weak interactions, QL–QL and QL–GeTe, respectively. In the present model, the bond length of Te^2 and Te^3 (see the atomic labels of Fig. 1) are 3.86 Å for $[(2,2_{)ref}]$ and 4.18 Å for $[(2,2)_{elng}]$, respectively. In contrast, the bond length of the two Te^2 atoms (the nearest neighboring Te atoms in the neighboring QLs) is 3.78 Å for $[(2,2)_{ref}]$, which is very close to that of $[(2,2)_{elng}]$, 3.71 Å. These findings suggest that bulk GST-SL of the $[(2,2)_{elng}]$ unit is a multilayer of $(QL)_2$ and $(GeTe)_2$ namely $(QL)_2/(GeTe)_2/(QL)_2/(GeTe)_2/(QL)_2/\ldots$ while that of $[(2,2)_{ref}]$ may be considered as a multilayer of $(QL)_1$ and $(QL)_1(GeTe)_2$ namely $(QL)_1(GeTe)_2/(QL)_1/(QL)_1(GeTe)_2/(QL)_1/\ldots$ by change of the relative bonding strength. Recall that not only simple QL bulk is a TI,[39,40] but also that [(1,2)] is ref. 28, Hence bulk GST-SL of [(2,2)] can be treated as multilayer of TI blocks and spacers (typically, NI), which segments neighboring TI blocks. They correspond to two different views: (1) $(QL)_2$ is the TI, and the spacer is $(GeTe)_2$; (2) $(QL)(GeTe)_2$ is the TI, and the spacer is $(QL)_1$.

We now move the focus to the 2D band dispersion of the interface states in the iPCM device. The contour plots of the density of states projected on the center QL of the RSL in the minimum device model, $W/[(2,2)_{ref}]_3(QL)_2/W$, are calculated for V = 0 volt and 0.5 volt, respectively. We find that the energy gap at the Γ-point, E_g, is 0.03 eV. The dispersion curves of the upper and lower interface band states are same sign quadratic curvatures in both cases. By increasing bias V from 0 to 0.5 volt, the interface bands are shifted up by about 0.05 eV in total. Here we note that the E_F of the device is the Fermi energy level of the W electrode, which in general is not equal to that of bulk GST-SL. In the case of zero bias, the central position of the energy gap at the Γ-point is close to E_F ($E \sim E_F - 0.03$ eV). By comparing with the surface states of GST-SL bulk, where the system breaks parity symmetry by facing vacuum, no clear Rashba split is found in the band dispersion of the interface states of the biased iPCM device. An applied bias 0.5 V is approximately equal to applying an electric field 0.05 eV nm^{-1} to the RSL, which is too weak to trigger the clear Rashba effect. The resulting contour plots are summarized in ESI (Fig. SI.1†).

Since the iPCM RSL consists of multilayers of TIs and NIs as outlined above, it is important to evaluate whether the iPCM device has functionalities corresponding to a topological phase change device or not. We therefore analyze the value of E_g for the interface states. In order to minimumize the effects of the hybridization of the electronics states of the electrodes and to extract intrinsic property of the interface states in the RSL, we took the device models $W/[(2,2)_{ref}]_9(QL)_2/W$ and $W/[(2,2)_{elng}]_9(QL)_2/W$. The density of states projected on the QL at the center of the RSL is calculated. We find that the energy gap is closing gradually by elongating the distance of the QL and the GeTe layers in the RSL ($[(2,2)_{ref}]_l \rightarrow [(2,2)_{elng}]_l$), while E_g is already very small ($E_g \sim 0.02$ eV) for $W/[(2,2)_{ref}]_9(QL)_2/W$. The curvature of the nearly degenerated upper and lower bands is also getting sharp (cusp-like). Furthermore, the expected Dirac point is almost pinned to E_F of the electrode. This agreement of Dirac point and the electrode E_F is potentially useful because the energy alignment to the electrode E_F determines functions of device. The details of the calculated contour plots of the interface states are shown in Fig. 4(c).

As stated above, the topological property of the surface state depends on the cleaved surface for [(2,2)] bulk. However, there is no physical cleaving facing vacuum when the $[(2,2)]_l$ film is used as RSL. We therefore analyze the topological phase transition of the RSL by analyzing the band energy gap of the interfaces states. We introduce a model Hamiltonian for 3D TI/NI multilayers, which is a slight extension of the model reported in ref. 30 and 31. This approach is valid when the thickness of the RSL is sufficiently large (*i.e.* l is a large number). We further extend the model to show the effects of each electronic coupling. First, we introduce the following Hamiltonian to present the isolated top (+) and bottom (−) interface states of each TI block of the RSL,

$$H = \sum_{k_\parallel}\sum_i [\nu_F \tau^z(\sigma^x k_y - \sigma^y k_x) + \Delta_{in}\tau^x] c^\dagger_{ik_\parallel} c_{ik_\parallel} + \sum_{k_\parallel}\sum_i \varepsilon_0 d^\dagger_{ik_\parallel} d_{ik_\parallel} + \Delta_{inter}\sum_{k_\parallel}\sum_{\pm}\sum_{\langle ij\rangle} \tau^{\pm} c^\dagger_{ik_\parallel} d_{jk_\parallel} + (\text{C.C}) \quad (1)$$

where σ^α, τ^α are Pauli matrices acting on the spins and on the top/bottom pseudospin states of the TI block, respectively. In order to simplify the notation we set the energy of the Dirac point to zero. The label i (j) is the index of the TI block or spacer. Only the direct interaction between the neighboring TI blocks and spacers is considered: thus the sum over $\langle ij\rangle$ indicates that i and j relate to neighboring TIs and spacers. The operators c ($c^\dagger$) represent annihilation (creation) operators for the interface states of the TI block, and d ($d^\dagger$) represent the analogous operators for states of the spacer between TI blocks, which work as "bridge sites". The first term in eqn (1) consists of the edge states of both sides in the same TI block and the interaction between them, whose transfer integral is Δ_{in}. The second term is for the 2D band confined in the bridge site, which typically is a NI.

The energy ε_0 is the difference between the energy of the Dirac point and the energy of the bridge site. The final term represents interaction between the states of the TI and the

nearest neighboring bridge site, where the transfer integral Δ_{inter} corresponds to the interlayer interaction of the neighboring TI and bridge site, and (C.C) denotes the Hermitian conjugate. When the bridge site can be treated as a perturbation, the Hamiltonian in eqn (1) can be further simplified to become[30,31]

$$H \simeq H^{\text{eff}} = \sum_{k_\parallel}\sum_{i}[\nu_F\tau^z(\sigma^x k_y - \sigma^y k_x) + \Delta_{\text{in}}\tau^x]c^\dagger_{ik_\parallel}c_{ik_\parallel} + \Delta^{\text{eff}}_{\text{inter}}\sum_{k_\parallel}\sum_{\pm}\sum_{\langle ij\rangle}\tau^{\pm}c^\dagger_{ik_\parallel}c_{jk_\parallel} \quad (2)$$

where we have introduced the effective transfer integral, $\Delta^{\text{eff}}_{\text{inter}} = \Delta^2_{\text{inter}}/\varepsilon_0$. Then the scaled energy gap E_g/Δ_{in} is expressed as $E_g/\Delta_{\text{in}} = 2|1 - XY|$ where $X = \Delta_{\text{inter}}/\Delta_{\text{in}}$ and $Y = \Delta_{\text{inter}}/\varepsilon_0$.[41] Following the discussion in the references of ref. 30 and 31, the sign of $1 - XY$ relates to the topological phase. When the sign is negative (positive), the energy gap of the multilayer is caused by topologically non-trivial (trivial) gapped states.

We can now apply the above analytical model to our NEGF-DFT results. We introduce the parameter Δ_{Q_1}, as is the interaction of the top and bottom edge states of one QL, and Δ_{NN}, as is the van der Waals interaction between neighboring stacked layers such as QL and GeTe or QL and QL. Firstly, we consider the calculated result for the W/[(2,2)$_{\text{elng}}$]$_9$(QL)$_2$/W system. As stated above, the RSL can be considered as a multilayer made of (QL)$_2$ as TIs, and of (GeTe)$_2$ as spacers. Since the coupling between the top and bottom edge states of the (QL)$_m$ block is proportional to $(\Delta_{Q_1})^m/(\Delta_{NN})^{m-1}$, Δ_{in} is equal to $(\Delta_{Q_1})^2/\Delta_{NN}$, and Δ_{inter} is equal to Δ_{NN}, respectively. Here, the energy gap scaled by Δ_{Q_1} is written as $E_g/\Delta_{Q_1} = \frac{2}{A}|1 - A^2B|$, where the parameters A and B are the relative interaction Δ_{NN}/Δ_{Q_1} and the scaled transfer integral $\Delta_{NN}/\varepsilon_0$, respectively. In the contrast, we now consider the W/[(2,2)$_{\text{ref}}$]$_9$(QL)$_2$/W RSL is a multilayer of (QL)$_1$(GeTe)$_2$ = TI and (QL)$_1$ = bridge site. Hence, the scaled energy gap is represented by $E_g/\Delta_{Q_1} = 2B|1 - A|$. As a result, we can construct a phase diagram to represent the energy gap and topological phase of the RSL, as presented in Fig. 5. There are two possible lines (conditions) to predict a Dirac semi-metal phase. While the applicable model will depend on the details of the change of the relative chemical bond characterized by strain, we can determine the generally valid properties. For an instance, both the parameters, A and B, are changed by strain. When the GST-SL is compressed, vW gap is rapidly compressed: thus the parameters A and B are linearly increased. The effective topological phase boundaries (white solid and dot lines in Fig. 5) depends on the initial state and chemical interaction to define the type of multilayer such as TI = (QL)$_2$, space = (GeTe)$_2$ or TI = (QL)$_1$(GeTe)$_2$, space = (QL)$_1$.

It is important to determine whether the discussed topological phase transitions in the RSL, and the related energy gap closing and opening, affect the performance of the nonvolatile memory or device. To this aim we evaluate the transmission coefficient $T\left(E, \vec{k}_\parallel\right)$ at the Γ point. The transmission coefficient represents the transmission probability of an electron

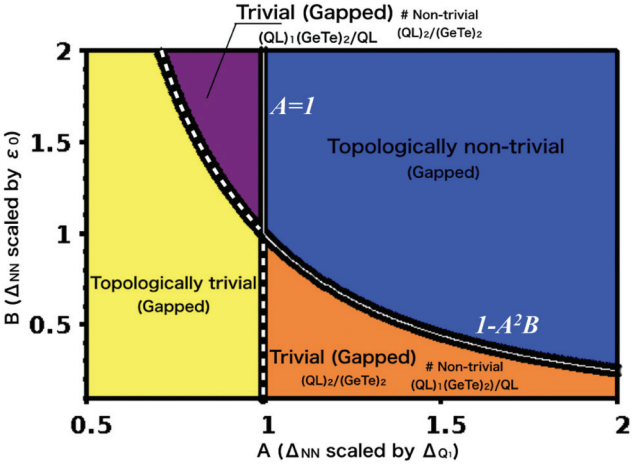

Fig. 5 The topological phase diagram of RSL [(2,2)]$_l$ plotted as a function of the parameters A (relative strength of interactions Δ_{NN}/Δ_{Q_1}) and B (scaled transfer integral by the energy difference of the neighboring QL and GeTe sites $\Delta_{NN}/\varepsilon_0$ of the bridge site). The thick black solid lines indicate the condition of Dirac semi-metal phase when TI is (QL)$_2$ and bridge is (GeTe)$_2$ (thick line) and TI is (QL)$_1$(GeTe)$_2$ and bridge is QL (thin line), respectively. The white solid and dot lines on the thick black lines are possible boundaries of the topological phase transition paths of RSL, respectively.

through the RSL with its energy E, hence, it relates to the wavefunctions of the electric transport channels between the source and drain electrodes. When the energy is close to E_F, the transmission coefficient is typically lower than 1.0×10^{-6} around the Γ point for the inverted Petrov phase. Then $T\left(E, \vec{k}_\parallel\right)$ at $E \sim E_F$ increases as one moves away from the Γ point to larger lateral $\vec{k}_\parallel$ values, as demonstrated in Fig. SI.2 of the ESI.† This tendency is similar with the cases of Ferro-GeTe and Petrov phases. These findings show that the electric conduction channel close to E_F of the iPCM device is not dominated by the wavefunctions at the Γ point. In particular, the wavefunction near Γ point of the inverted Petrov phase have only small electron density at vW gap in the GeTe block or QL/electrode interface although it is delocalized on the QL blocks in the device. It can be conductive along the direction parallel to the surface. Thus coexistence of the property of HRS as iPCM and the gapless Dirac semimetal, which is responsible to 2D interfacial transport, does not conflict at all. The electronic structure close to the Γ point does not play an important role in the resistive switching function, so that the topological nature of the interface states is not directly related to the functionality nonvolatile memory. The $\vec{k}_\parallel$ dependence and high resistance of the electronic state at Γ point of the IP structure can be shown more directly by analysis of the electric resistance at each lateral $\vec{k}_\parallel$ point. We compare the zero-bias resistance of the IP structure (HRS: R_{HRS}) calculated by using the values of only each $\vec{k}_\parallel$ point region close M, Γ, and K point, respectively. The result is summarized as follows. The IP structure, the ratio of $R_{\text{HRS}}(K)/R_{\text{HRS}}(\Gamma)$ is 0.9, while $R_{\text{HRS}}(M)/R_{\text{HRS}}(\Gamma)$ is only 0.01. Note that all of the $R_{\text{HRS}}(M)$, $R_{\text{HRS}}(\Gamma)$, and $R_{\text{HRS}}(K)$ are much larger than that of LRS of FGT(vl)

structure as expected. For an instance, the ratio $R_{HRS}(\Gamma)/R_{LRS}$ is 3.5×10^{-4}.

In order to activate the Dirac semi-metallic phase in a novel functional device, one has to (1) change the structure of the cell to activate the electron transport in the 2D plane or (2) to design contacts to connect the interface states of the RSL and conduction channels in the electrode at the Γ point. Multi-layered devices obtained by inserting buffer metallic layer at the contact can be a promising approach. However, in such a renewed device, the relation of the structural phases and the HRS/LRS can be somewhat different. As an example, let us focus on the P(v) structure. This provides a better connection of the channel wavefunctions in neighboring QL blocks than that of the IP. This means that the energy alignment of the QL block and the GeTe layer improves by changing to the P(v) structure, which corresponds to decreasing the parameter B. According to the phase diagram, the better energy alignment enhances the energy gap at the Dirac point. If the dominant conduction channels is located near the Dirac point, the P(v) will not be necessarily the LRS for the present transport direction.

Summary

In the present paper, we study the I–V characteristics of iPCM device cells in the low voltage regime by using NEGF-DFT and including SO interaction, and examine possible crystalline phases of the GST-SL in order to identify HRS and LRS. The I–V calculations indicate that a two-step dynamical process, which consists of vertical flips and lateral motions of the Ge and Te atoms, is key to obtain bias polarity-dependence of SET/RESET modes. For such a two-step mechanism, both the Petrov and the Ferro-GeTe phases are candidates as possible LRSs. Because of the symmetric structure of $(GeTe)_2$ in the former phase, the switching is expected to be independent of the bias-polarity. On the contrary, the resulting GeTe sequences of the latter phase (*i.e.*, Te–Ge–Te–Ge or Ge–Te–Ge–Te) must depend on the bias polarity. We emphasize that the effects of the SO interaction provide largely different electric currents between the two Ferro-GeTe conformations, which include a vertical flip without or with lateral motion. For the lateral motion we presently consider it to be induced by thermal relaxation processes after the field/current-induced vertical flip motion. In this case the resistive switching speed depends on the relaxation time. In the contrast, only Petrov phases are suitable for the LRS when a one-step dynamics is assumed. Since a field-driven mode is usually preferred to design ultra-low power and fast switching memories, the evaluation of the time-scales of the thermal relaxation in the Ferro-GeTe phase and of the Joule heating to trigger vertical flips are required. This is a challenging task and a question open to future studies.

We also analyze the 2D interface states inside the iPCM device. By rigorous first-principles calculations of the Green's functions, the energy gap of the Ferro-GeTe phase at the Γ point is found to be larger than that of the inverted Petrov phase. This is due to the Rashba effect. The additionally induced Rashba effect with an applied voltage is found to be too weak to lead to significant changes in the conductance. By varying the inter layer distance of Sb_2Te_3 blocks and $(GeTe)_2$ layers, the energy gap of the interface states of the inverted Petrov phase is gradually closing. Changing the inter layer distance might be achieved in experiments by arranging mechanically the gap distance of the electrodes, for example also by including piezoelectric elements in the device. However, the topological property is not directly related to the functionality of the present nonvolatile memory, because there is a mismatch between the Dirac point and the k-point of the most conductive channel of the leads.

Method

All DFT calculations were performed using the SIESTA package,[42] and the NEGF-DFT transport calculations were then performed using the Smeagol code,[33,34] as well as HiRUNE subroutines[32] developed in-house for data analysis. We used the local density approximation (LDA) for the exchange–correlation (XC) functional. Single zeta plus polarization function (SZP) level basis set was adopted for W atom while we used double zeta plus polarization function (DZP) for the other atoms. We included SO interactions to perform NEGF-DFT calculations, while they were not included to determine atomic structures of device models. We took a $16 \times 16 \times 1$ Monkhorst–Pack k-point sampling to determine the density matrix of the iPCM device cell, while $16 \times 16 \times 1$ and $16 \times 16 \times 16$ were used for the present GST-SL and W bulk calculations, which were used to evaluate surface Green's functions and lead self-energies. To obtain convergence of the I–V characteristics as well as of the transmission coefficients, a finer k-point sampling is required. In the present study we took 100×100 k-points after getting the converged density matrix by NEGF-DFT. In the 0-bias approximation, we use the converged density matrix of the equilibrium state, and then calculated the transmission coefficient and obtained the I–V characteristics by integrating the transmission coefficient over the voltage-dependent bias window. In the fully self-consistent NEGF calculation, the chemical potentials of left/right electrodes shift up/down by $V/2$ from their equilibrium value, and a self-consistent calculation to determine density matrix is performed for each bias. Thus the effect of the voltage drop between the electrodes is explicitly included.

Acknowledgements

This work was supported by CREST, JST (Grant No. JPMJCR14F1). IR acknowledges financial support from the EU H2020 programme PETMEM project (Grant No. 688282). SS acknowledges financial support from Science Foundation Ireland (Grant No. 14/IA/2624).

References

1 S. Mittal and J. S. Vetter, *IEEE Trans. Parallel Distrib. Syst.*, 2016, **27**(5), 1537–1550.
2 S. Raoux, in *Advances in Non-volatile Memory and Storage Technology*, ed. Y. Nishi, Woodh. Pub. Ser. Elect., 2014, pp. 161–199.
3 S. Raoux, F. Xiong, M. Wuttig and E. Pop, *MRS Bull.*, 2014, **39**(8), 703–710.
4 M. Chen, K. A. Rubin and R. W. Barton, *Appl. Phys. Lett.*, 1986, **49**(9), 502–504.
5 N. Yamada, E. Ohno, N. Akahira, K. Nishiuchi, K. Nagata and M. Takao, *Jpn. J. Appl. Phys., Part 1*, 1987, **26**, 61–66.
6 M. Hase and J. Tominaga, *Proc. SPIE*, 2012, **8260**.
7 R. E. Simpson, P. Fons, A. V. Kolobov, T. Fukaya, M. Krbal, T. Yagi and J. Tominaga, *Nat. Nanotechnol.*, 2011, **6**(8), 501–505.
8 J. Tominaga, A. V. Kolobov, P. J. Fons, X. M. Wang, Y. Saito, T. Nakano, M. Hase, S. Murakami, J. Herfort and Y. Takagaki, *Sci. Technol. Adv. Mater.*, 2015, **16**(1), 014402.
9 J. Tominaga, R. E. Simpson, P. Fons and A. V. Kolobov, *Appl. Phys. Lett.*, 2011, **99**(15), 152105.
10 T. Shintani, S. Soeya and T. Saiki, *ECS Trans.*, 2014, **64**(14), 69–74.
11 X. M. Yu and J. Robertson, *Sci. Rep.*, 2016, **6**, 22353.
12 S. Soeya and T. Shintani, *J. Appl. Phys.*, 2012, **112**(3), 034301.
13 J. Kalikka, X. L. Zhou, E. Dilcher, S. Wall, J. Li and R. E. Simpson, *Nat. Commun.*, 2016, **7**, 11983.
14 J. Momand, R. N. Wang, J. E. Boschker, M. A. Verheijen, R. Calarco and B. J. Kooi, *Nanoscale*, 2015, **7**(45), 19136–19143.
15 K. Makino, S. Kuromiya, K. Takano, K. Kato, M. Nakajima, Y. Saito, J. Tominaga, H. Iida, M. Kinoshita and T. Nakano, *ACS Appl. Mater. Interfaces*, 2016, **8**(47), 32408–32413.
16 K. Makino, Y. Saito, K. Mitrofanov, J. Tominaga, A. V. Kolobov, T. Nakano, P. Fons and M. Hase, *Springer Proc. Phys.*, 2015, **162**, 199–201.
17 B. Huang and J. Robertson, *Phys. Rev. B: Condens. Matter*, 2012, **85**(12), 125305.
18 L. Bolotov, Y. Saito, T. Tada and J. Tominaga, *Sci. Rep.*, 2016, **6**, 33223.
19 T. Ohyanagi, M. Kitamura, M. Araidai, S. Kato, N. Takaura and K. Shiraishi, *Appl. Phys. Lett.*, 2014, **104**(25), 252106.
20 A. Caretta, B. Casarin, P. Di Pietro, A. Perucchi, S. Lupi, V. Bragaglia, R. Calarco, F. R. L. Lange, M. Wuttig, F. Parmigiani and M. Malvestuto, *Phys. Rev. B: Condens. Matter*, 2016, **94**(4), 045319.
21 J. Tominaga, A. V. Kolobov, P. Fons, T. Nakano and S. Murakami, *Adv. Mater. Interfaces*, 2014, **1**(1), 1300027.
22 H. Nakamura and Y. Asai, *Phys. Chem. Chem. Phys.*, 2016, **18**(13), 8820–8826.
23 H. Nakamura, Y. Asai, J. Hihath, C. Bruot and N. J. Tao, *J. Phys. Chem. C*, 2011, **115**(40), 19931–19938.
24 D. Bang, H. Awano, J. Tominaga, A. V. Kolobov, P. Fons, Y. Saito, K. Makino, T. Nakano, M. Hase, Y. Takagaki, A. Giussani, R. Calarco and S. Murakami, *Sci. Rep.*, 2014, **4**, 05727.
25 K. Makino, Y. Saito, P. Fons, A. V. Kolobov, T. Nakano, J. Tominaga and M. Hase, *Appl. Phys. Lett.*, 2014, **105**(15), 151902.
26 X. M. Yu and J. Robertson, *Sci. Rep.*, 2015, **5**, 12612.
27 T. A. Nguyen, D. Backes, A. Singh, R. Mansell, C. Barnes, D. A. Ritchie, G. Mussler, M. Lanius, D. Grutzmacher and V. Narayan, *Sci. Rep.*, 2016, **6**, 27716.
28 B. S. Sa, J. Zhou, Z. M. Sun, J. Tominaga and R. Ahuja, *Phys. Rev. Lett.*, 2012, **109**(9), 096802.
29 Y. Takagaki, Y. Saito and J. Tominaga, *Appl. Phys. Lett.*, 2016, **108**(11), 112102.
30 A. A. Burkov and L. Balents, *Phys. Rev. Lett.*, 2011, **107**(12), 127205.
31 G. B. Halasz and L. Balents, *Phys. Rev. B: Condens. Matter*, 2012, **85**(3), 035103.
32 H. Nakamura, K. Yamashita, A. R. Rocha and S. Sanvito, *Phys. Rev. B: Condens. Matter*, 2008, **78**(23), 235420.
33 A. R. Rocha, V. M. Garcia-Suarez, S. Bailey, C. Lambert, J. Ferrer and S. Sanvito, *Phys. Rev. B: Condens. Matter*, 2006, **73**(8), 085414.
34 I. Rungger and S. Sanvito, *Phys. Rev. B: Condens. Matter*, 2008, **78**, 035407.
35 M. Liebmann, C. Rinaldi, D. Di Sante, J. Kellner, C. Pauly, R. N. Wang, J. E. Boschker, A. Giussani, S. Bertoli, M. Cantoni, L. Baldrati, M. Asa, I. Vobornik, G. Panaccione, D. Marchenko, J. Sanchez-Barriga, O. Rader, R. Calarco, S. Picozzi, R. Bertacco and M. Morgenstern, *Adv. Mater.*, 2016, **28**(3), 560–565.
36 J. G. Checkelsky, Y. S. Hor, R. J. Cava and N. P. Ong, *Phys. Rev. Lett.*, 2011, **106**(19), 196801.
37 D. Di Sante, P. Barone, R. Bertacco and S. Picozzi, *Adv. Mater.*, 2013, **25**(4), 509–513.
38 Y. Asai and H. Fukuyama, *Phys. Rev. B: Condens. Matter*, 2005, **72**(8), 085431.
39 L. He, X. F. Kou and K. L. Wang, *Phys. Status Solidi RRL*, 2013, **7**(1–2), 50–63.
40 D. Hsieh, Y. Xia, D. Qian, L. Wray, F. Meier, J. H. Dil, J. Osterwalder, L. Patthey, A. V. Fedorov, H. Lin, A. Bansil, D. Grauer, Y. S. Hor, R. J. Cava and M. Z. Hasan, *Phys. Rev. Lett.*, 2009, **103**(14), 146401.
41 M. A. Ratner, *J. Phys. Chem.*, 1990, **94**(12), 4877–4883.
42 J. M. Soler, E. Artacho, J. D. Gale, A. Garcia, J. Junquera, P. Ordejon and D. Sanchez-Portal, *J. Phys.: Condens. Matter*, 2002, **14**(11), 2745–2779.